# Pharmacokinetics and Dosimetry of an α-Particle Emitter Labeled Antibody: $^{213}$Bi-HuM195 (Anti-CD33) in Patients with Leukemia

George Sgouros, Åse M. Ballangrud, Joseph G. Jurcic, Michael R. McDevitt, John L. Humm, Yusuf E. Erdi, Bipin M. Mehta, Ronald D. Finn, Steven M. Larson and David A. Scheinberg

*Department of Medical Physics, Radiology and Medicine, Memorial Sloan-Kettering Cancer Center, New York, New York; and Pharm-Actinium, Chevy Chase, Maryland*

Data from nine patients with leukemia participating in a phase I activity-escalation study of HuM195, labeled with the α-particle emitter $^{213}$Bi (half-life = 45.6 min), were used to estimate pharmacokinetics and dosimetry. This is the first trial using an α-particle emitter in humans. The linear energy transfer of α particles is several hundredfold greater than that of β emissions. The range in tissue is approximately 60–90 μm. **Methods:** The activity administered to patients ranged from 0.6 to 1.6 GBq. Patient imaging was initiated at the start of each injection. Thirty 1-min images followed by ten 3-min images were collected in dynamic mode; a 20% photopeak window centered at 440 keV was used. Blood samples were collected until 3 h postinjection and counted in a gamma counter. Contours around the liver and spleen were drawn on the anterior and posterior views and around a portion of the spine on the posterior views. No other organs were visualized. **Results:** The percentage injected dose in the liver and spleen volumes increased rapidly over the first 10–15 min to a constant value for the remaining hour of imaging, yielding a very rapid uptake followed by a plateau in the antibody uptake curves. The kinetic curves were integrated to yield cumulated activity. The mean energy emitted per nuclear transition for $^{213}$Bi and its daughters, adjusted by a relative biologic effectiveness of 5 for α emissions, was multiplied by the cumulated activity to yield the absorbed dose equivalent. Photon dose to the total body was determined by calculating a photon-absorbed fraction. The absorbed dose equivalent to liver and spleen volumes ranged from 2.4 to 11.2 and 2.9 to 21.9 Sv, respectively. Marrow (or leukemia) mean dose ranged from 6.6 to 12.2 Sv. The total-body dose (photons only) ranged from $2.2 \times 10^{-4}$ to $5.8 \times 10^{-4}$ Gy. **Conclusion:** This study shows that patient imaging of $^{213}$Bi, an α-particle emitter, labeled to HuM195 is possible and may be used to derive pharmacokinetics and dosimetry. The absorbed dose ratio between marrow, liver and spleen volumes and the whole body for $^{213}$Bi-HuM195 is 1000-fold greater than that commonly observed with β-emitting radionuclides used for radioimmunotherapy.

**Key Words:** radioimmunotherapy; α particle; $^{213}$Bi; HuM195; leukemia

**J Nucl Med 1999; 40:1935–1946**

Received Aug. 17, 1998; revision accepted Apr. 9, 1999.

For correspondence or reprints contact: George Sgouros, PhD, Department of Medical Physics, Memorial Sloan-Kettering Cancer Center, 1275 York Ave., New York, NY 10021.

In targeting disseminated disease in which individual clonogenic cells or cell clusters may be found in isolation, a radionuclide that is capable of sterilizing individual cells without a dose contribution from adjacent cells is required (*1,2*). The probability that a particular radionuclide will be capable of single-cell sterilization depends on the specific activity of the radiolabeled antibody and the number of antigen sites on the cell surface. β-Particle-emitting radionuclides are currently prevalent in radioimmunotherapy because they have shown partial efficacy against larger volume disease (*3*). Given achievable specific activities for radiolabeled antibodies and commonly observed antigen-site densities on the surface of tumor cells, radionuclides with emissions that exhibit a substantially greater linear energy transfer (LET) than that of β particles are required for single-cell kill. The LET of α particles is 400 times greater than that of β particles (80 versus 0.2 keV/μm). Each traversal of an α particle through the nucleus results in a highly ionizing track. Cell survival studies have shown that cell death may result from as few as one to three α-particle tracks across the nucleus (*4–8*).

Most studies with α-particle-emitting radionuclides for therapy have examined either $^{212}$Bi (*8*) or $^{211}$At (*9–11*). Both radionuclides are short lived, with 61-min and 7.2-h half-lives, respectively, and emit α particles with ranges of 40–90 μm. $^{212}$Bi decay is also accompanied by the emission of high-energy (2.6 MeV) photons. In preclinical studies of rapidly accessible, disseminated disease, these radionuclides have shown a significant curative potential with minimal toxicity (*8,12*).

$^{213}$Bi has a half-life of 45.6 min and a branched decay scheme similar to that of $^{212}$Bi, but without the high yield of energetic and potentially hazardous photon emissions (*13–17*). The dosimetry and pharmacokinetic analyses used in this study were derived from the first clinical trial using $^{213}$Bi in humans (*18*).

HuM195 is a recombinant humanized version of the mouse antibody M195. M195 is an IgG2a mouse monoclonal antibody, reactive with CD33, an antigen with restricted

expression on myeloid and monocytic leukemia cells, myeloid progenitors and monocytes (*19,20*). Antigen density is 10,000 and 5,000 sites per cell on myeloid and monocytic leukemia cells and mature monocytes, respectively. A series of phase I and II trials using M195 and HuM195 (*21–23*) for treatment of myeloid leukemia has shown that M195 antibodies rapidly and efficiently target and saturate leukemia cell sites, followed subsequently by internalization of the radioconjugate into the target cells. Measurements of M195 antibody internalization performed ex vivo showed 30%–50% of bound M195 antibody internalized into leukemia cells over 2–4 h. Internalized antibody was retained within the cells for variable amounts of time (*22*).

Treatment using a short-lived α-particle emitter requires an understanding of antibody pharmacokinetics and dosimetry that may not be extrapolated from experience obtained using $^{131}$I-labeled antibody therapy (*24*). $^{131}$I has been the predominant radionuclide for antibody therapy (*3,25*). The half-life of $^{131}$I is 8 d, and the therapeutic effect is obtained from absorption of β particles with an average range in tissue of approximately 470 μm (*26,27*). Because of its long half-life, absorbed dose estimates for $^{131}$I-labeled antibodies require pharmacokinetic information that spans a period of several days. Loss of the radionuclide is determined predominantly by biologic clearance rather than physical decay. In contrast, the pharmacokinetic period relevant for the dosimetry of $^{213}$Bi-labeled antibodies is measured in minutes and hours rather than days.

The purpose of this study was to demonstrate patient imaging with $^{213}$Bi, an α-particle emitter, labeled to HuM195, and to describe in patients with myeloid leukemia the methodologies implemented for pharmacokinetics and dosimetry.

## MATERIALS AND METHODS

### Clinical Trial

Details regarding trial design, patient population and radiochemistry may be found in published reports (*16,18*). Briefly, patients with relapsed acute myeloid leukemia received total administered activities ranging from 0.6 to 1.6 GBq (16–43 mCi) $^{213}$Bi-HuM195. Cumulative amounts of administered activity of 10.4, 15.5 and 20.7 MBq/kg defined dose levels 1–3, respectively. $^{213}$Bi-HuM195 was administered by intravenous push over 5 min, with patients positioned under a dual-head gamma camera. Because of constraints on the specific activity that may be achieved for any one injection, radioactivity dose escalation was performed by increasing the number of injections to keep the specific activity constant. The number of injections ranged from 3 to 6 over a 48-h period.

### Phantom Imaging

Before patient imaging, phantom studies were performed to assess the feasibility of imaging $^{213}$Bi and to select the optimum acquisition conditions for patient studies (*28*). The decay scheme for $^{213}$Bi is depicted in Figure 1; 16.5% of $^{213}$Bi decays are accompanied by a 440-keV photon emission. Phantom studies were performed by imaging the 440-keV photopeak using a 20% energy window. A line (3 mm outer diameter) and disk source (4 cm diameter) containing 15 and 26 MBq (0.4 and 0.7 mCi), respectively, were imaged for 30 min. Both high-energy, general-purpose (HEGP) and high-energy, high-resolution (HEHR) collimation was used. Imaging was performed on Genesys gamma cameras (ADAC, Inc., Milpitas, CA). The high-voltage gain on the camera detectors was reduced to allow imaging at 440 keV.

When HEGP collimation was used, images of the line and disk sources showed a "star" artifact associated with septal penetration of high-energy photons. This artifact also created the impression of activity foci within the uniform line source. Images obtained with HEHR collimation did not show such a pronounced artifact but were of lower sensitivity. Because the artifacts seen on the HEGP images could influence interpretation of bone marrow uptake along the spine, the HEHR collimator was chosen for use in human studies, despite the reduction in sensitivity. A sensitivity of 200 cpm/MBq (8000 cpm/mCi) and a full width at half maximum of 1.3 cm were obtained using this collimator.

### Patient Imaging

Patient imaging was performed on a Vertex gamma camera (ADAC). Based on the results of the phantom study, HEHR collimation was used (*28*). Immediately before patient imaging, a

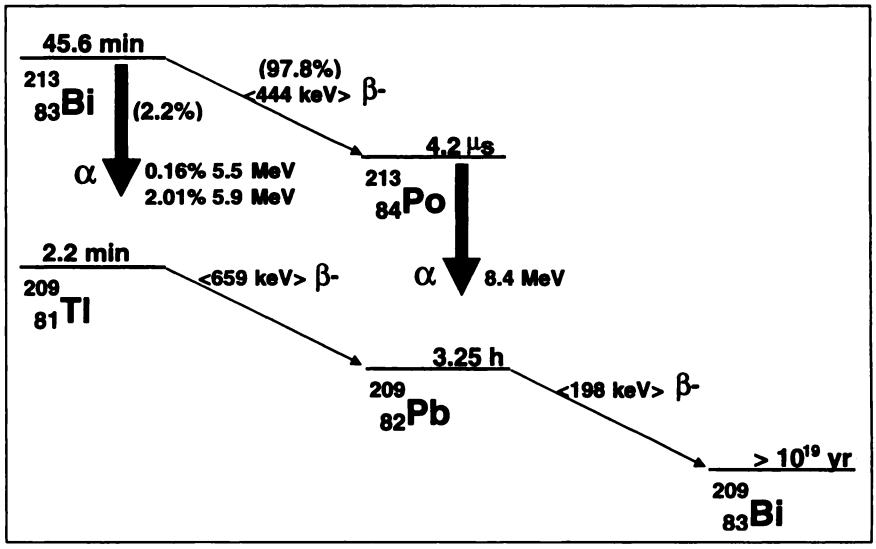


**FIGURE 1.** $^{213}$Bi decay scheme (adapted from Browne et al. [*27*]).

photopeak window, centered around 440 keV and with a 20% width, was set using a $^{213}$Bi standard. A scatter window abutting the lower energy side of the 440-keV window and of equal absolute width was also set (*29,30*). One half of the counts from this window was subtracted from the photopeak window to yield scatter-corrected images. This approach to scatter correction was taken from the method described by Jaszczak et al. (*29*) for $^{99m}$Tc, as adapted by Koral et al. (*30*). A value of 0.7 was reported by Koral et al. (*30*) for $^{131}$I. To ensure that no information was lost from images already low in counts, we used a factor of 0.5. The actual factor depends on the activity distribution, and, given the lack of availability and short half-life of $^{213}$Bi, phantom studies were not performed specifically to derive this factor for different activity distributions. Therefore, we chose to use the factor of 0.5 only to improve visualization and to define regions of interest (ROIs) that were then applied to photopeak window images. As indicated below, an adjacent background region that was scaled by pixel number was used to subtract background and scatter from organ or tumor ROI counts obtained from the photopeak image.

Using a dual-head gamma camera, anterior and posterior images were obtained simultaneously. Images were collected in dynamic mode, with a collection duration for each frame of 1 min for the first 30 min and 3 min for the last 30 min. The patients were injected while positioned in the camera; imaging began at the start of injection. Because the pharmacokinetics of $^{213}$Bi-HuM195 at early times were not known, the imaging protocol was designed to allow adequate resolution in time and the ability to obtain adequate counting statistics by summing images over appropriate time intervals. At the end of patient imaging, a calibrated standard of approximately 7.4 MBq (200 μCi) was imaged for 5 min with the same detector and couch positions as used for imaging the patient.

Contours (ROIs) around the liver, spleen and an extended marrow region (vertebra T11–L5) were drawn as illustrated in Figure 2. An ROI encompassing 7 vertebra was used to represent the marrow to obtain a better representation of overall marrow uptake. A single image was used for contour drawing. This was obtained by summing the last ten 3-min images after they had been scatter corrected. The contours were placed on the basis of the organ outline as visually determined on the images. These contours were then transposed onto the dynamic photopeak image sets and used to extract the total number of counts in each region at each time point postinjection. The counts obtained in each region were corrected for background by drawing ROIs adjacent to each organ.

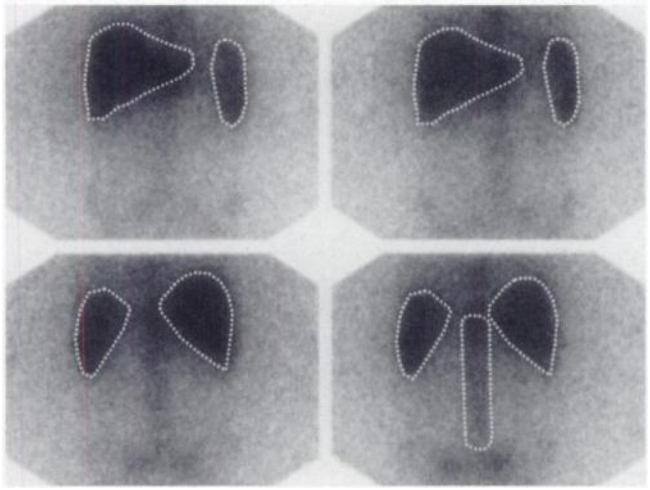

**FIGURE 2.** Anterior (top row) and posterior (bottom row) patient images showing contours used to identify liver, spleen and red marrow region. Images after second and fourth injection are shown.

The activities in the liver and spleen were determined as the geometric mean of the counts per minute in the anterior and posterior images, given by:

$$C_{ORG} = \sqrt{\frac{CA_{ORG}}{PA_{ORG}} \times \frac{CP_{ORG}}{PP_{ORG}}} \times PW_{ORG}, \quad \text{Eq. 1}$$

where $C_{ORG}$ equals the conjugate view cpm in the organ; $CA_{ORG}$ and $CP_{ORG}$ are the cpm in the ROIs in the anterior and posterior images, respectively; $PA_{ORG}$ and $PP_{ORG}$ are the number of pixels in the organ ROI in the anterior and posterior image, respectively; and $PW_{ORG}$ equals the total number of pixels obtained when drawing a contour around the whole organ. For the liver, PW equals PA. The spleen visualized in the posterior image is larger than in the anterior image, so PW equals PP. Background activity was determined by calculating the geometric mean of the background cpm:

$$C_{BKG} = \sqrt{\frac{CA_{BKG}}{PA_{BKG}} \times \frac{CP_{BKG}}{PP_{BKG}}} \times PW_{ORG} \times BTF, \text{ and} \quad \text{Eq. 2}$$

$$BTF = \frac{T_{WB} - T_{ORG}}{T_{WB}}, \quad \text{Eq. 3}$$

where the same notation is used as for the organ activity. BTF represents a background thickness factor that scales background counts according to organ thickness ($T_{ORG}$) relative to whole-body thickness ($T_{WB}$), which was measured at the time of imaging. Liver thickness was determined from patient CT images. When CT scans were not available, liver thickness was estimated on the basis of the size of the liver relative to the size and thickness of the liver of a patient for whom a CT scan was available. Spleen thickness was obtained using the minor axis value estimated in obtaining the spleen volume. Details are provided in the dosimetry section.

Because of constraints on available camera time, attenuation corrections were performed analytically, rather than by transmission measurements. The cpm for liver and spleen were corrected for background counts and tissue attenuation and were converted to radioactivity using the following:

$$A_{ORG} = (C_{ORG} - C_{BKG}) \times \frac{AttCorr}{C_{STD}}, \quad \text{Eq. 4}$$

$$C_{STD} = \frac{\sqrt{CA_{STD} \times CP_{STD}}}{A_{STD}}, \text{ and} \quad \text{Eq. 5}$$

$$AttCorr = e^{\mu(T_{WB}-T_{ORG})/2} \times \frac{\mu \times T_{ORG}}{2 \times \text{Sinh}(\mu \times T_{ORG}/2)}. \quad \text{Eq. 6}$$

$CA_{STD}$ and $CP_{STD}$ are the anterior and posterior cpm obtained from the calibration standard. $A_{STD}$ is equal to the activity of $^{213}$Bi in the standard. AttCorr is an organ-specific attenuation correction factor, determined by the organ thickness ($T_{ORG}$), the whole-body thickness ($T_{WB}$) and the attenuation coefficient. An attenuation coefficient of $\mu = 0.10$ cm$^{-1}$ was used for 440-keV photons (*31*). Both organ self-attenuation and attenuation associated with tissue between the organ surface and the body surface are accounted for by Equation 6.

Activity in the spine region was estimated from the posterior view only, using the following equations:

$$C_{SPINE} = CP_{SPINE}, \quad \text{Eq. 7}$$

$$C_{BKG\text{-}SPINE} = \frac{1}{2} \times \left[\left(\frac{CP_{BKG}}{PP_{BKG}}\right)_{LIVER} + \left(\frac{CP_{BKG}}{PP_{BKG}}\right)_{SPLEEN}\right] \times PW_{SPINE}, \quad \text{Eq. 8}$$

$$A_{SPINE} = (C_{SPINE} - C_{BKG-SPINE}) \times \frac{AttCorr_{SPINE}}{C_{STD-SPINE}}, \quad \text{Eq. 9}$$

$$C_{STD-SPINE} = \frac{CP_{STD}}{A_{STD}}, \quad \text{Eq. 10}$$

$$AttCorr_{SPINE} = e^{\mu \times d}. \quad \text{Eq. 11}$$

As depicted in Equation 11, self-attenuation was assumed to be negligible for counts originating in the spine. Parameter d is the distance between the spine and the posterior surface of the body and was determined from the patient's CT scan, when available. When CT scans were not available, d was estimated on the basis of the patient's weight relative to other patients for whom parameter d could be measured on CT scans.

Equations 1–11 were applied to each frame to yield kinetic data, A(t), for each of the regions over the 60-min imaging period. The kinetic curves were decay corrected to the time of injection and converted to percentage injected dose (%ID) in each region:

$$A(t)_{DecayCorr} = A(t) \times e^{\ln 2 \times t/45.6}, \text{ and} \quad \text{Eq. 12}$$

$$\%ID(t) = \frac{A(t)_{DecayCorr}}{IA} \times 100, \quad \text{Eq. 13}$$

where IA is the activity injected at the start of imaging (t = 0).

The %ID for the spine ROI was converted to marrow %ID by scaling a nominal estimate of the red marrow mass in vertebra T11–L5 according to body weight (*32*).

### Blood Sampling

After the first and last injections, serial blood samples were collected from each patient at 5, 10, 15, 30, 45, 60, 90, 120 and 180 min. Aliquots of both whole-blood and plasma samples were counted. Whole blood was centrifuged for 2 min at 2000 rpm to obtain plasma. All samples were counted for 1 min in a gamma counter (Compugamma model 1282; LKB Wallac, Gaithersburg, MD) that had been calibrated previously for $^{213}$Bi. The data were decay corrected to the time of injection and expressed as percentage of injected activity per liter.

### Dosimetry

All time-activity data, A(t), were fitted to a sum or difference of two exponentials, the latter if there was an uptake component to the time-activity data:

$$A_{fit}(t) = A_1 \times e^{-t/T_1} \pm A_2 \times e^{-t/T_2}. \quad \text{Eq. 14}$$

These expressions were then integrated analytically to yield the cumulated activity, $\tilde{A}$ (i.e., total number of decays), within each region or organ (*33*). Liver volumes were determined from patient CT scans; when CT scans were not available, they were estimated on the basis of the number of pixels in the liver ROI relative to the size of the liver ROI of a patient for whom a CT scan was available. In patients with leukemia, the spleen volume is not reliably predicted by scaling a standard spleen volume. Volume estimates of the spleen were obtained by assuming that the organ may be represented as an ellipse (*34*). The major and minor axes, a and b, respectively, were determined from the $^{213}$Bi images by measuring the long and short axes of the spleen. The third axis, perpendicular to the imaging plane, was assumed to be equal to the minor axis. The boundaries were visually determined from the radioactivity distribution; therefore, the length of the axes will be underestimated because the true boundary extends beyond that determined from the activity distribution (*35*). A correction for this was made by assuming that the true axes are longer by a fixed fraction (f) of the measured axes. This assumption yields:

$$V = \frac{\pi}{6} \times (a + fa)(b + fb)^2, \quad \text{Eq. 15}$$

which reduces to:

$$V = \frac{\pi}{6} \times ab^2 \times (1 + f)^3. \quad \text{Eq. 16}$$

By setting the spleen volume obtained using Equation 16, with a and b known from the $^{213}$Bi images, equal to a volume estimate obtained from CT, a value of 0.22 was obtained for f. This value translates to a threshold value for contour drawing that is consistent with values that have been estimated and reported elsewhere (*36*). The corrected minor axis was also used as the spleen thickness in Equations 3 and 6.

Volumes were converted to masses assuming unit density. The cumulated activity for each volume ($\tilde{A}$) was divided by the mass of each organ to give cumulated activity concentration. Mean absorbed doses to liver and spleen volumes and to the red marrow were obtained by multiplying the cumulated activity concentration in each organ by the mean energy emitted per nuclear transition, $\Delta$, for the electron and $\alpha$-particle emissions of $^{213}$Bi and its daughters. The individual contributions of each daughter for electrons are shown in Table 1; corresponding values for $\alpha$-particle emissions are listed in Table 2.

An absorbed fraction of 1 was assumed for both electron and $\alpha$-particle irradiation. The absorbed dose from photons to activity-containing organs was assumed to be negligible relative to the electron and $\alpha$-particle dose. A relative biologic effectiveness of 5 for cellular inactivation was assumed for $\alpha$ particles (*37*). The effective mean energy emitted per nuclear transition is, therefore: $\Delta = 1.05 \times 10^{-13}$ Gy-kg/Bq-s + $5 \times 1.33 \times 10^{-12}$ Gy-kg/Bq-s = $6.76 \times 10^{-12}$ Sv-kg/Bq-s. The absorbed dose, D, obtained using the methods described above, yields an average over the organ volume:

$$D = \frac{\tilde{A}}{M_{ORG}} \times (\Delta_e + 5 \times \Delta_\alpha), \quad \text{Eq. 17}$$

where $M_{ORG}$ is the organ mass.

The photon dose to the whole body ($D_{WB}$) was calculated as the product of the total amount administered ($A_0$) and the whole-body to whole-body S-factor ($S_{WB \leftarrow WB}$), divided by the decay constant ($\lambda$) of $^{213}$Bi:

$$D_{WB} = \frac{A_0}{\lambda} \times S_{WB \leftarrow WB} \quad \text{Eq. 18}$$

$$\lambda = \frac{\ln(2)}{T_{1/2}}. \quad \text{Eq. 19}$$

The parameter $T_{1/2}$ is equal to the half-life of $^{213}$Bi.

**TABLE 1**
Electron Emissions Considered in Absorbed Dose Calculations

| | Electrons | | | | | |
|---|---|---|---|---|---|---|
| Isotope | Energy (keV) | Isotope % per disintegration | Effective % per disintegration | Mean energy (keV/disintegration) | $\Delta_e$ (Gy-kg/Bq-s) | Electron range (mm) |
| $^{213}$Bi | 200 | 0.20 | 0.20 | 0.40 | 6.41E-17 | 0.5 |
| $^{213}$Bi | 347 | 2.55 | 2.55 | 8.85 | 1.42E-15 | 1.4 |
| $^{213}$Bi | 423 | 0.40 | 0.40 | 1.69 | 2.71E-16 | 1.9 |
| $^{213}$Bi (beta) | 444 | 97.80 | 97.80 | 434.23 | 6.96E-14 | 2.1 |
| $^{209}$Tl (beta) | 659 | 100.00 | 2.20 | 14.50 | 2.32E-15 | 4.2 |
| $^{209}$Pb (beta) | 198 | 100.00 | 100.00 | 198.00 | 3.17E-14 | 0.5 |
| Total | | | | 657.67 | 1.05E-13 | |

$\Delta_e$ = electron energy emitted per nuclear transition of $^{213}$Bi.

The implicit assumption in using these equations is that all administered activity decays within the body. This assumption is appropriate given the short half-life of $^{213}$Bi.

The whole-body to whole-body S-factor for $^{213}$Bi ($S_{WB \leftarrow WB}$) was obtained as the product of the photon absorbed fraction and the yield for each of the relevant photons in the decay chain of $^{213}$Bi, divided by 70 kg, the reference man value for whole-body mass (*34,38*). Table 3 lists the photons that were considered and the corresponding S-factor values (*27*). The sum yields $S_{WB \leftarrow WB}$ for $^{213}$Bi.

Organs that did not concentrate $^{213}$Bi-HuM195 were assigned the whole-body photon dose. The electron absorbed dose was estimated by apportioning the cumulated activity concentration in blood according to each organ's blood volume. The resulting organ cumulated activities were then divided by the mass of each organ. Nominal organ blood volumes and masses (*32*) were scaled by each patient's whole-body weight. Absorbed dose estimates were obtained by multiplying the cumulated activity concentration in each organ by the mean energy emitted per nuclear transition for electron emissions (Table 1). These assumptions yielded the average absorbed dose to each organ, assuming a uniform distribution of radioactivity throughout each organ's mass. The dose contributions due to electrons from the β decay of $^{213}$Bi to $^{213}$Po and from $^{209}$Pb to $^{209}$Bi (stable) were estimated separately. Estimates were performed for the heart, kidneys and lungs.

The absorbed dose to blood was calculated by analytically integrating the fitted expression obtained from the pharmacokinetic analysis of serial blood samples. This yielded the cumulated activity concentration in the blood, $[\tilde{A}]_{BL}$. Assuming a blood density of 1 g/cm$^3$, the average absorbed dose to blood was obtained as the product of the mean energy emitted per nuclear transition, Δ, for electron and α-particle emissions of $^{213}$Bi and its daughters (Tables 1 and 2), and $[\tilde{A}]_{BL}$.

In most patients, pharmacokinetic data were collected only after the first and last injections. Absorbed doses or dose equivalents for injections for which no data were collected were estimated by weighted averaging of the known values. In estimating an unknown value, the weight assigned to known values depended on the number of injections elapsed between the two estimates. Known values that were closer in injection number to the unknown value were given a greater weight.

The short half-life of $^{213}$Bi precluded the collection and analysis of bone marrow biopsies over a relevant time period. Biopsy-based stochastic or microdosimetric analyses of the absorbed dose or specific energy distribution within cellular target volumes in the marrow were not performed. A conventional Medical Internal Radiation Dose approach to estimating the absorbed dose to tumor cells in regions that yielded enough counts for imaging was appropriate because of the large number of α-particle emissions in such regions and the associated increase in energy deposition to cell nuclei from cross-fire (*1*).

## RESULTS

### Imaging

The contours used to assess liver, spleen and red marrow kinetics are shown on Figure 2. The percentages of administered activity that localized to the red marrow, liver and

**TABLE 2**
α-Particle Emissions Considered in Absorbed Dose Calculations

| | α particles | | | | | |
|---|---|---|---|---|---|---|
| Isotope | Energy (keV) | Isotope % per disintegration | Effective % per disintegration | Mean energy (keV/disintegration) | $\Delta_\alpha$ (Gy-kg/Bq-s) | α-Particle range (μm) |
| $^{213}$Bi | 5549 | 0.16 | 0.16 | 8.88 | 1.42E-15 | 42.0 |
| $^{213}$Bi | 5869 | 2.01 | 2.01 | 117.97 | 1.89E-14 | 45.5 |
| $^{213}$Po | 7614 | 0.003 | 0.003 | 0.22 | 3.58E-17 | 66.0 |
| $^{213}$Po | 8375 | 100.00 | 97.80 | 8190.75 | 1.31E-12 | 75.6 |
| Total | | | | 8317.82 | 1.33E-12 | |

$\Delta_\alpha$ = α-particle energy emitted per nuclear transition of $^{213}$Bi.

**TABLE 3**
Individual Photon S-Factors and Summed Photon S-Factor Used for $^{213}$Bi Photon Dosimetry

| Isotope | Photon energy (keV) | S-factor (Gy/MBq-s) |
|---|---|---|
| $^{213}$Bi | 440 | 5.78E-11 |
| $^{213}$Bi | 79 | 9.84E-13 |
| $^{209}$Tl | 117 | 1.60E-12 |
| $^{209}$Tl | 467 | 6.71E-12 |
| $^{209}$Tl | 1566 | 2.37E-11 |
| Total = $S_{WB-WB}$ | | 9.08E-11 |

$S_{WB-WB}$ = whole-body to whole-body S-factor.

spleen are depicted as a function of time for patients 2, 5 and 8 in Figure 3. No localization to kidneys or urinary bladder was observed. The number of patients who showed an increase, decrease and no change in liver activity with increasing injections was 1, 7 and 1, respectively. Corresponding numbers for spleen were 1, 3 and 5, and for marrow 4, 3 and 2. A tendency toward decreased uptake in liver with increasing injection number, therefore, was evident. The red marrow, liver and spleen regions accounted for 70% to >100% of the administered activity. In some cases, the sum exceeded 100% because the activity concentration measured in the marrow ROI was assumed to be constant throughout the marrow. Depending on the distribution of the disease, this could be an overestimate (*39*). All curves were characterized by a 5- to 10-min rise followed by a plateau at a level that was constant throughout the remaining 60 min of imaging. No dose-related effect was apparent. The kinetic curves associated with red marrow exhibit a greater variability than those for liver or spleen because the counts in the ROI used to represent whole red marrow were lower and therefore subject to a greater statistical uncertainty than those in liver or spleen (Fig. 2). This is especially the case for the first 30 min of imaging, in which 1-min frames were collected.

### Blood Kinetics

Antibody clearance curves for whole blood and plasma are depicted in Figure 4 for patients 2, 5 and 8. In some patients, a rapid initial drop in antibody concentration was observed over the first 10–20 min. Beyond 40 min and throughout the remaining 3 h of sample collection, antibody clearance from blood was negligible for all patients. A similar pattern was observed for plasma. The intercepts, or estimated initial distribution volumes, in plasma and blood were similar for all patients, suggesting that a significant fraction of the activity in blood was associated with cellular elements. Clearance rates did not depend on the number of injections administered. After 20 min postinjection, the activity concentration in blood or plasma after the last injection was unchanged for 1 patient and exceeded that after the first injection for 8 patients. An increase in activity concentration in blood or plasma after multiple injections was consistent with a saturation effect. There was no consistent increase in blood or plasma concentration across patients, however, relative to the total amount of antibody administered. No clear relationship could be discerned between the clearance curves for marrow, liver and spleen and those of plasma and blood.

### Dosimetry

The absorbed dose equivalents per administered activity to blood, red marrow, liver and spleen are summarized in Table 4, which also lists the total amount of radionuclide and antibody administered to each patient. This was generally divided over the number of injections given. Estimated values were used when measurements were not made to provide an average dose per injection. The average absorbed dose equivalent per injection is provided. The dose equivalent to red marrow also represents the mean dose to leukemia cells. It is especially important to note that because the liver and spleen may also contain targeted leukemia cells, the absorbed doses calculated for these organ volumes will overestimate the actual dose to normal organ parenchyma. Given the short range of $^{213}$Bi $\alpha$ emissions, accurate estimation of the absorbed dose to these tissues would require knowledge of the spatial distribution of $^{213}$Bi decays on a cellular level. That the average dose over the organ volume is an overestimate is confirmed by the absence of hepatic toxicity in all patients (*18*).

Figures 5 and 6 examine possible relationships between the absorbed dose estimates listed in Table 4 and the administered antibody. As shown in Figure 5, the absorbed dose equivalent to red marrow decreased as the administered antibody increased. The change in absorbed dose between the first (or second, in the case of patient 2) and last injections is plotted against administered antibody in Figure 6. Both red marrow and spleen exhibit a relationship between these two parameters. The shapes of the red marrow and spleen curves are similar. This similarity is likely to reflect targeting of leukemia and normal CD33$^+$ cells in the spleen. In one patient (patient 9, at 3 mg administered antibody), the percent increase in absorbed dose to the marrow was much greater than to the spleen. This "outlier" may be explained by a positive slope in the red marrow time-activity curves for this patient after the fifth injection (data not shown). This was not present for the first injection. This apparent increase in antibody uptake over time yielded a much greater red marrow absorbed dose after the fifth injection relative to the first. No relationship between absorbed dose and administered antibody was seen for the blood or liver.

Absorbed doses to the whole body and to the heart, kidneys and lungs, organs that did not concentrate $^{213}$Bi-HuM195, are listed in Table 5. The whole-body dose is composed of only photon emissions. Because of the short half-life of $^{213}$Bi, excretion from the body was assumed to be negligible, and the whole-body residence time, therefore, was the same for all patients. The whole-body dose per amount injected activity, therefore, was the same for each

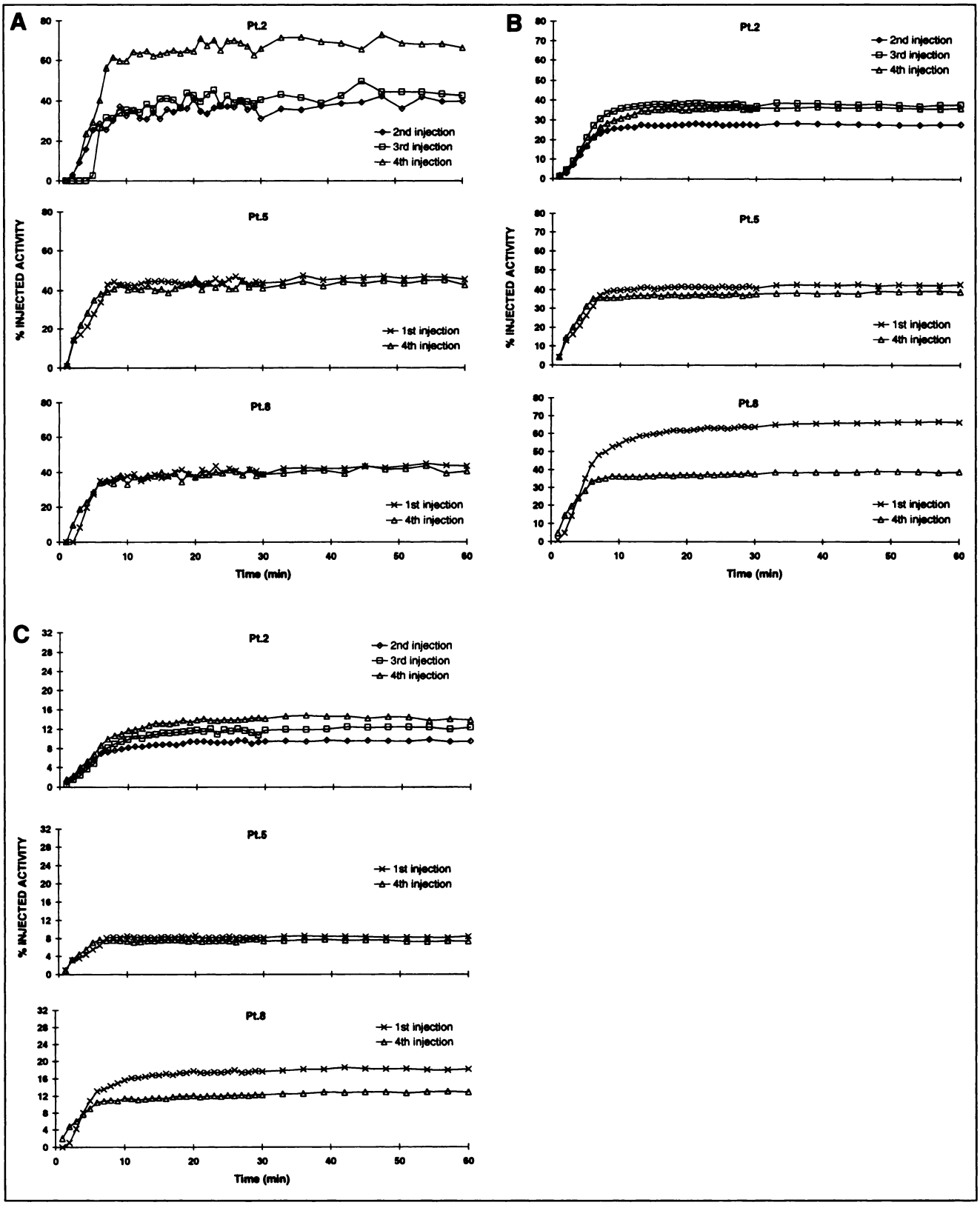


**FIGURE 3.** Time-activity curves obtained from red marrow (A), liver (B) and spleen (C) for patients 2, 5 and 8. Red marrow region, as shown in Figure 2, is scaled to represent total marrow.

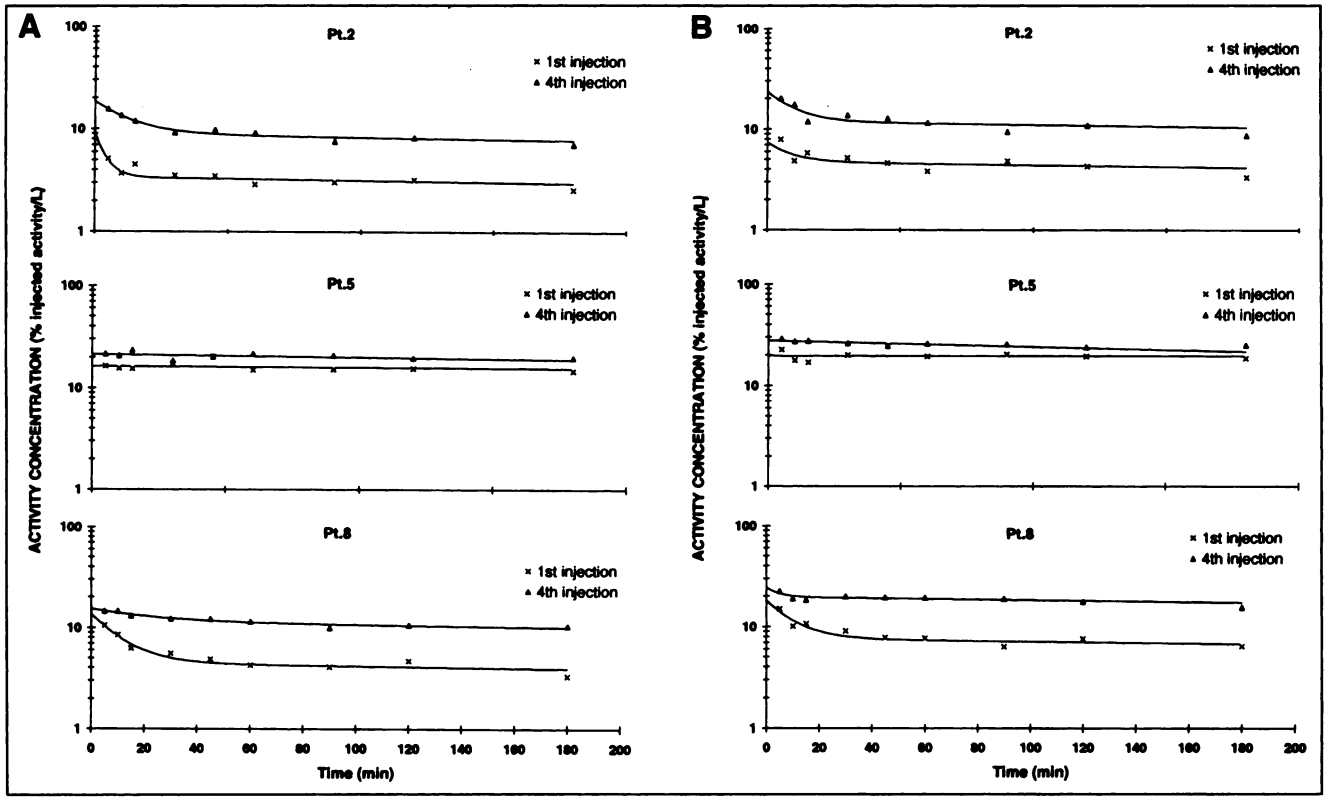


**FIGURE 4.** Time-activity curves obtained from blood (A) and serum (B) for patients 2, 5 and 8 after first and last injections.

patient, $3.6 \times 10^{-4}$ mGy/MBq. The total dose listed for each organ was the sum of the photon (or whole-body) dose and the electron dose. The contributions from $^{213}$Bi and $^{209}$Pb to the electron dose are tabulated separately. All dose values in Table 5 are in units of mGy/MBq rather than mSv/MBq, because the dose associated with α emissions, and therefore a factor associated with relative biologic effectiveness, is not incorporated.

## DISCUSSION

The pharmacokinetics of an α-particle-emitting radionuclide, $^{213}$Bi, labeled to a humanized, anti-CD33 antibody, HuM195, have been measured in patients with leukemia. Absorbed dose estimates to normal and target organs have been performed. The concentration of $^{213}$Bi-HuM195 in red marrow, liver and spleen increased rapidly during injection and then remained at or close to its maximum value throughout the remaining 60 min of imaging. Because of the rapid decay of the radionuclide and the need to monitor possible kidney uptake, whole-body images were not obtained. The absorbed dose equivalent delivered to the red marrow after 600–1600 MBq (16–43 mCi) $^{213}$Bi-HuM195 ranged from 656 to 1220 cSv.

Because leukemia is characterized by an unregulated proliferation of hematopoietic cells or blasts in the bone marrow, targeting to marrow is predominantly the result of antibody binding to leukemia cells. The mean absorbed dose to the marrow volume, therefore, also reflects the dose delivered for treatment. Proliferation and infiltration of leukemia cells to extramedullary sites are also common. The liver and spleen are common sites because they are both highly vascularized organs. The extent to which the mean absorbed dose to these organs may also be considered as the dose to leukemia will depend on the tumor burden in each organ, its distribution within the organ, the distribution of the radionuclide and the range of its emissions. Correspondingly, the absorbed dose to the blood will also reflect targeting of circulating blasts, the concentration of which will vary with each patient.

This study provides an opportunity to examine the early biodistribution of administered antibody as the antibody protein level increases. Such information may also be used for modeling and for treatment optimization (*24*). The blood and plasma curves for most patients show a higher concentration of antibody in the corresponding volumes after the last administration relative to the first. The blood data are much less susceptible to the uncertainties associated with the planar imaging-derived organ data. If the absorbed dose to each organ is plotted against administered amount of antibody (Fig. 5), a trend toward decreasing average absorbed dose per administered antibody is seen for the red marrow, and an increase is seen for the liver. The dose to blood will depend on peripheral cell count density and, therefore, may not follow the antibody-dose relationship

**TABLE 4**
Absorbed Dose Equivalents per Unit Administered Activity

| | Patient no. | | | | | | | | |
|---|---|---|---|---|---|---|---|---|---|
| | 1 | 2 | 3 | 4 | 5 | 6 | 7 | 8 | 9 |
| Patient information | | | | | | | | | |
| Activity/body weight (MBq/kg) | 11.4 | 11.2 | 11.1 | 16.2 | 15.7 | 14.2 | 18.4 | 20.8 | 21.3 |
| Activity (MBq) | 807 | 602 | 605 | 876 | 1083 | 1613 | 924 | 1312 | 1343 |
| Administered antibody (mg) | 1.7 | 1.6 | 1.8 | 1.7 | 3.0 | 4.4 | 2.5 | 3.6 | 3.0 |
| | Absorbed dose estimates (mSv/MBq) | | | | | | | | |
| Blood | | | | | | | | | |
| 1st injection | 1.4 | 1.0 | 1.9 | 4.4 | 4.3 | 0.8 | 2.4 | 1.5 | 1.5 |
| 2nd injection | 1.4* | 1.0* | 1.9* | 4.4* | 4.3* | 0.8* | 2.7* | 1.5* | 1.5* |
| 3rd injection | 1.7* | 2.7* | 2.4* | 4.6* | 5.6* | 1.0* | 2.9 | 3.2* | 2.2* |
| 4th injection | 1.7 | 2.7 | 2.4 | 4.6* | 5.6 | 1.0* | | 3.2 | 2.9* |
| 5th injection | | | | 4.8* | | 1.1* | | | 2.0 |
| 6th injection | | | | 4.8 | | 1.1 | | | |
| Average† | 1.5 (121) | 1.8 (108) | 2.2 (133) | 4.6 (403) | 4.9 (531) | 1.0 (161) | 2.7 (249) | 2.3 (302) | 2.2 (295) |
| Red marrow | | | | | | | | | |
| 1st injection | 9.3 | 9.0* | 10.7 | 10.0 | 7.9 | 5.8 | 13.0 | 8.9 | 5.4 |
| 2nd injection | 8.0* | 9.0 | 10.4 | 11.2 | 7.9* | 5.8* | 13.2* | 8.9* | 5.4* |
| 3rd injection | 6.7 | 10.8 | 10.8 | 11.2* | 7.6* | 5.1* | 13.5 | 8.0* | 7.9* |
| 4th injection | 14.7 | 15.0 | 11.5 | 12.2* | 7.6 | 5.1* | | 8.0 | 10.3* |
| 5th injection | | | | 13.2* | | 4.4* | | | 10.3 |
| 6th injection | | | | 13.2 | | 4.4 | | | |
| Average† | 9.7 (783) | 10.9 (656) | 10.9 (659) | 11.8 (1034) | 7.8 (845) | 5.1 (823) | 13.2 (1220) | 8.4 (1102) | 7.9 (1061) |
| Liver | | | | | | | | | |
| 1st injection | 6.5 | 3.7* | 4.4 | 5.6 | 6.6 | 5.6 | 4.3 | 10.7 | 6.8 |
| 2nd injection | 5.7* | 3.7 | 4.3 | 5.5 | 6.6* | 5.6* | 4.1* | 10.7* | 6.8* |
| 3rd injection | 4.8 | 4.9 | 3.9 | 5.5* | 6.2* | 4.7* | 4.0 | 6.3* | 5.4* |
| 4th injection | 4.3 | 4.7 | 3.4 | 5.5* | 6.2 | 4.7* | | 6.3 | 4.1* |
| 5th injection | | | | 5.5* | | 3.7* | | | 4.1 |
| 6th injection | | | | 5.5 | | 3.7 | | | |
| Average† | 5.3 (428) | 4.3 (259) | 4.0 (242) | 5.5 (482) | 6.4 (693) | 4.7 (758) | 4.1 (379) | 8.5 (1115) | 5.4 (725) |
| Spleen | | | | | | | | | |
| 1st injection | 13.4 | 7.6* | 4.7 | 19.1 | 5.3 | 4.2 | 9.7 | 16.3 | 17.4 |
| 2nd injection | 14.2* | 7.6 | 4.7 | 19.5 | 5.3* | 4.2* | 9.3* | 16.3* | 17.4* |
| 3rd injection | 15.0 | 10.0 | 4.8 | 19.5* | 4.8* | 3.8* | 8.9 | 12.4* | 16.3* |
| 4th injection | 16.3 | 11.0 | 4.8 | 20.0* | 4.8 | 3.8* | | 12.4 | 15.3* |
| 5th injection | | | | 20.5* | | 3.4* | | | 15.3 |
| 6th injection | | | | 20.5 | | 3.4 | | | |
| Average† | 14.7 (1186) | 9.0 (542) | 4.7 (290) | 19.8 (1734) | 5.0 (542) | 3.8 (613) | 9.3 (859) | 14.3 (1876) | 16.3 (2189) |

*Estimated value, obtained using methods described in text.
†Total dose equivalent (cSv) is given in parentheses.

seen in marrow. Absorbed dose estimates (but not pharmacokinetics) depend heavily on the estimates used for organ masses. When the confounding issue of mass estimation is removed, and an internal comparison is made, as in Figure 6, a relationship between marrow and spleen dose delivery may be observed, supporting the possibility that a significant fraction of splenic uptake reflects targeting of leukemia cells in the spleen. Figure 6 also shows that when the total administered antibody is approximately 2.5–3 mg, the first injection will deliver the same absorbed dose as the last. This may be the optimum milligram amount for therapy because, as shown in Figure 5, this is also the protein amount in which the liver absorbed dose begins to increase.

The absorbed dose to organs that did not concentrate $^{213}$Bi-HuM195 did not include α-particle emissions because, given their short range and the 45.6-min half-life of $^{213}$Bi, they would not contribute to normal organ dose. The dose associated with electrons was determined separately for $^{213}$Bi and $^{209}$Pb, the two radionuclides that would be expected to contribute significantly. $^{209}$Tl also emits electrons but at a relative yield of only 2%. $^{213}$Bi emits β particles with a mean energy of 444 keV and a yield of 97.8%. $^{209}$Pb, the common decay product of the two $^{213}$Bi daughters, emits β particles with a mean energy of 198 keV; it decays with a half-life of 3.25 h. Absorbed dose to organs that did not concentrate the antibody was obtained assuming

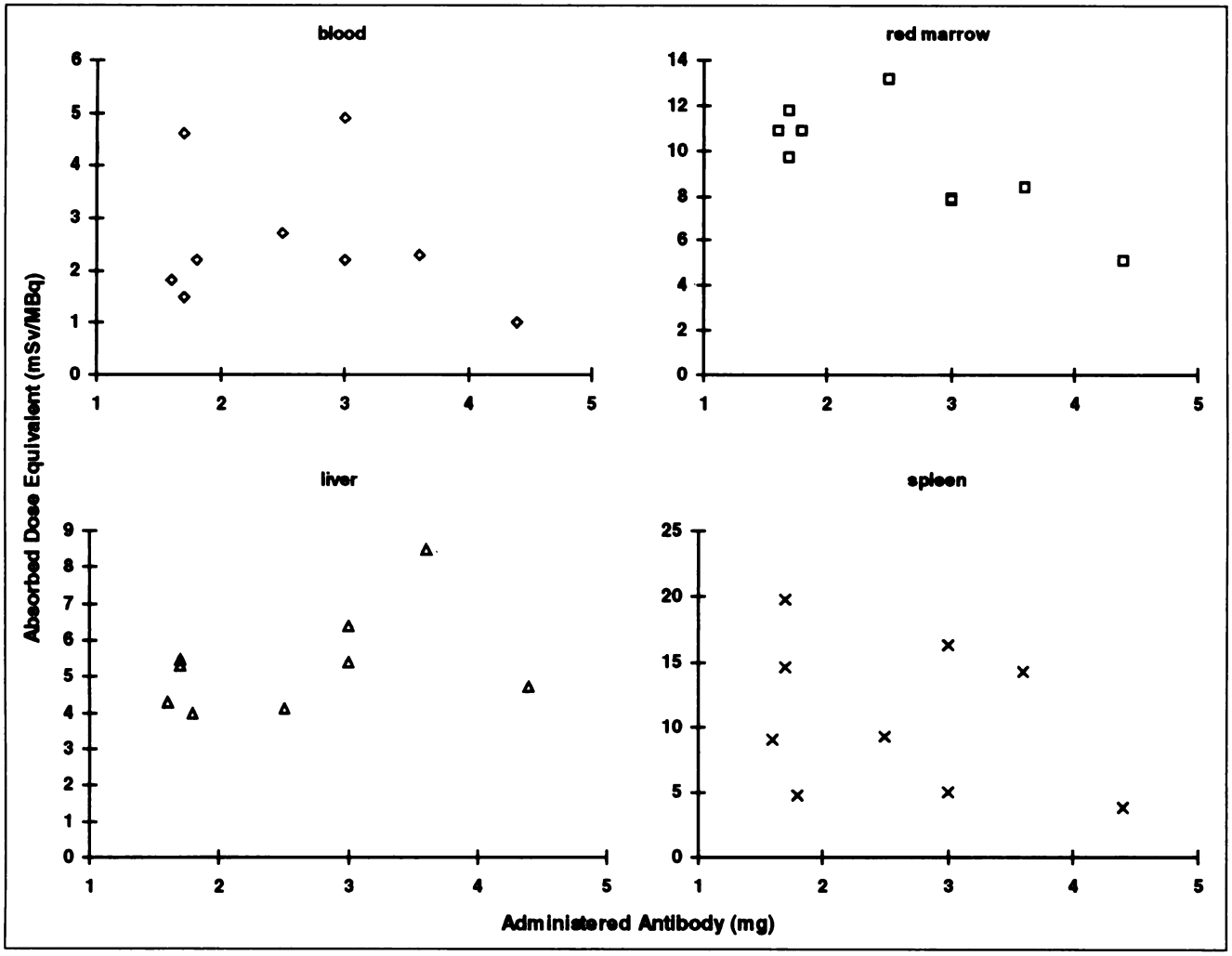


**FIGURE 5.** Absorbed dose equivalent to red marrow for each patient as function of amount (milligrams) of administered antibody.

uniform energy distribution. The validity of the uniform energy deposition assumption for $^{213}$Bi electron emissions depends on the degree to which the labeled antibody extravasates before transformation of the $^{213}$Bi and also on the range of the electron emissions. Given the short half-life of $^{213}$Bi, extravasation will be minimal. Transformation of $^{213}$Bi to $^{213}$Po, however, yields electron emissions with an average range of 5–10 mm. Even if confined to the vasculature, therefore, the electron emissions of $^{213}$Bi may irradiate a significant portion of normal tissue. The electron emissions of $^{209}$Pb have an average range of 0.5–1 mm. The 3.25-h half-life of $^{209}$Pb allows for extravasation and diffusion throughout a larger distribution volume. As biodistribution studies of lead have shown, however, this distribution volume will be confined largely to blood because lead rapidly localizes to red blood cells, where it binds to hemoglobin (*40*). In both cases, therefore, the electron absorbed dose estimates listed in Table 5 are derived from an assumption (i.e., uniform distribution of emitters throughout the organ volume) that oversimplifies the actual absorbed dose distribution.

## CONCLUSION

This study shows that patient imaging of $^{213}$Bi, an α-particle emitter, labeled to HuM195, is possible and may be used to derive pharmacokinetics and dosimetry. The absorbed dose ratio between marrow, liver and spleen volumes, sites known to harbor disease in patients with leukemia, and the whole body for $^{213}$Bi-HuM195 is 1000-fold greater than that commonly observed with β-emitting radionuclides used for radioimmunotherapy.

## ACKNOWLEDGMENTS

The authors thank Joanne D. Greene, Hovanes Kalaigian and Richard Schumacher for their technical and laboratory assistance. This work was supported, in part, by Department of Energy grant DE-FG02–86ER60407 and National Institutes of Health grants PO1 CA-33049, R01 CA-55349 and R01 CA-62444 and also by the Rich Foundation. Clinical grade $^{225}$Ac for $^{213}$Bi generation was provided by PharmActinium, Inc., Chevy Chase, MD; the Institute for Transuranic Elements, Karlsruhe University, Karlsruhe, Ger-

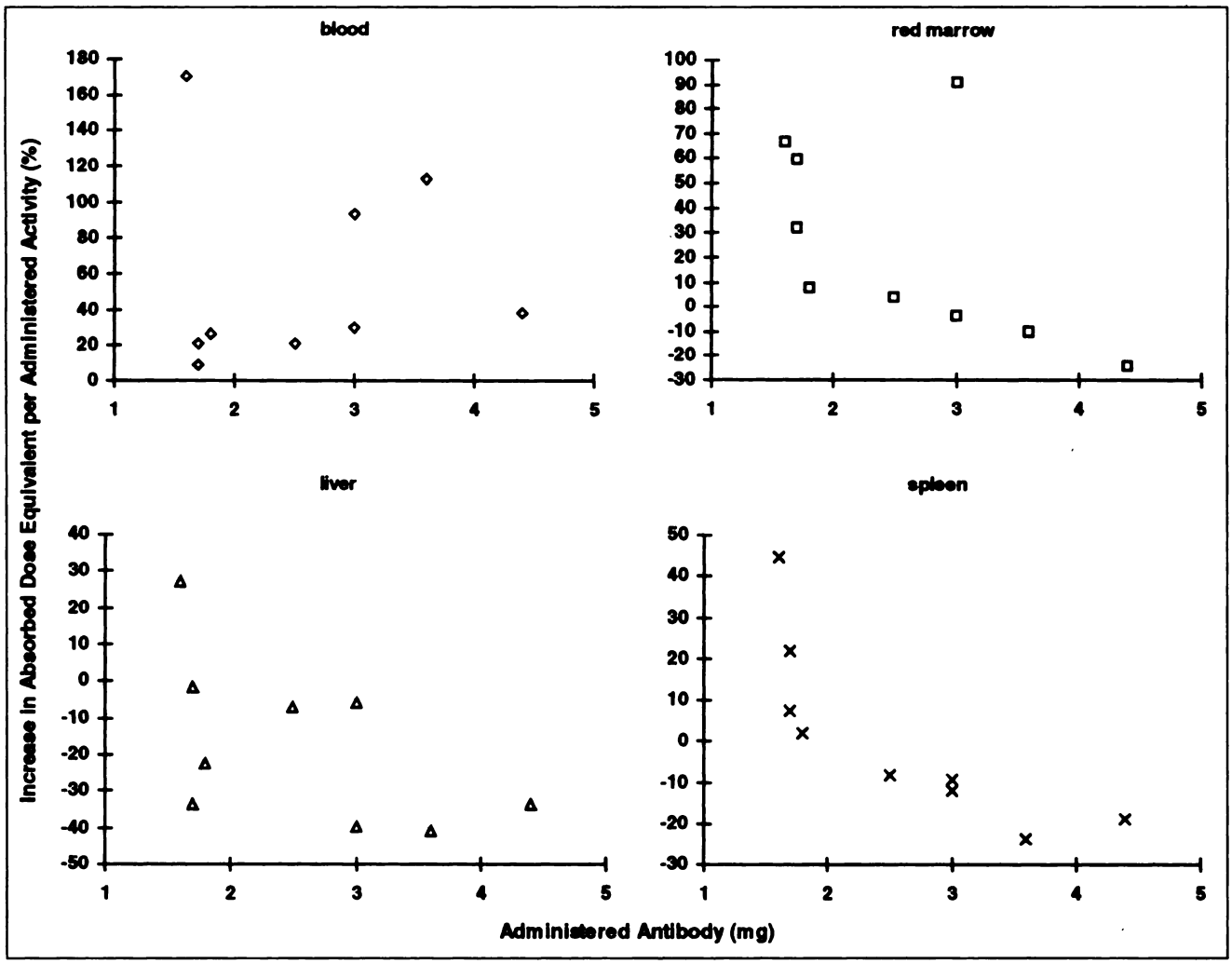


**FIGURE 6.** Effect on absorbed dose of multiple administrations. Percentage change in absorbed dose equivalent to blood, red marrow, liver and spleen arising from first versus last injection of antibody is plotted against total amount of administered antibody.

**TABLE 5**
Absorbed Dose Estimates for Normal Organs (Disease-Free Organs not Targeted by $^{213}$Bi-HuM195)

| Patient no. | Absorbed dose (mGy/MBq) | | | | | | | | |
|---|---|---|---|---|---|---|---|---|---|
| | Heart | | | Kidneys | | | Lungs | | |
| | $^{213}$Bi electrons | $^{209}$Pb electrons | Total* | $^{213}$Bi electrons | $^{209}$Pb electrons | Total* | $^{213}$Bi electrons | $^{209}$Pb electrons | Total* |
| 1 | 2.6E-03 | 1.2E-03 | 4.1E-03 | 3.7E-03 | 1.7E-03 | 5.7E-03 | 8.6E-03 | 3.9E-03 | 1.3E-02 |
| 2 | 2.3E-03 | 1.0E-03 | 3.6E-03 | 3.2E-03 | 1.4E-03 | 5.0E-03 | 7.4E-03 | 3.4E-03 | 1.1E-02 |
| 3 | 2.8E-03 | 1.3E-03 | 4.4E-03 | 3.9E-03 | 1.8E-03 | 6.0E-03 | 9.1E-03 | 4.1E-03 | 1.4E-02 |
| 4 | 5.9E-03 | 2.7E-03 | 8.9E-03 | 8.3E-03 | 3.8E-03 | 1.2E-02 | 1.9E-02 | 8.8E-03 | 2.9E-02 |
| 5 | 8.1E-03 | 3.7E-03 | 1.2E-02 | 1.1E-02 | 5.2E-03 | 1.7E-02 | 2.7E-02 | 1.2E-02 | 3.9E-02 |
| 6 | 2.6E-03 | 1.2E-03 | 4.1E-03 | 3.6E-03 | 1.7E-03 | 5.7E-03 | 8.6E-03 | 3.9E-03 | 1.3E-02 |
| 7 | 3.2E-03 | 1.4E-03 | 5.0E-03 | 4.4E-03 | 2.0E-03 | 6.8E-03 | 1.0E-02 | 4.8E-03 | 1.6E-02 |
| 8 | 3.9E-03 | 1.8E-03 | 6.0E-03 | 5.4E-03 | 2.5E-03 | 8.2E-03 | 1.3E-02 | 5.8E-03 | 1.9E-02 |
| 9 | 3.5E-03 | 1.6E-03 | 5.5E-03 | 5.0E-03 | 2.3E-03 | 7.6E-03 | 1.2E-02 | 5.3E-03 | 1.7E-02 |

*Whole-body photon dose of 0.00036 mGy/MBq is included in total organ estimates.

many; and the Department of Energy, Isotopes Production and Distribution. The authors also thank Maurits W. Geerlings, PhD, for his help in securing bismuth generators.

## REFERENCES


1. Humm JL. Dosimetric aspects of radiolabeled antibodies for tumor therapy. *J Nucl Med.* 1986;27:1490–1497.
2. Sgouros G. Radioimmunotherapy of micrometastases. In: Riva P, ed. *Cancer Radioimmunotherapy: Present and Future.* Harwood Academic Publishers; 1998: 191–207.
3. Larson SM, Sgouros G, Cheung NKV. Monoclonal antibodies in cancer therapy: radioisotope conjugates. In: Devita VT, Hellman S, Rosenberg SA, eds. *Biologic Therapy of Cancer.* 2nd ed. Philadelphia, PA: Lippincott; 1995:534–552.
4. Humm JL. A microdosimetric model of astatine-211 labeled antibodies for radioimmunotherapy. *Int J Radiat Oncol Biol Phys.* 1987;13:1767–1773.
5. Humm JL, Chin LM. A model of cell inactivation by alpha-particle internal emitters. *Radiat Res.* 1993;134:143–150.
6. Kozak RW, Atcher RW, Gansow OA, Friedman AM, Hines JJ, Waldmann TA. Bismuth-212-labeled anti-Tac monoclonal antibody: alpha-particle-emitting radionuclides as modalities for radioimmunotherapy. *Proc Natl Acad Sci USA.* 1986;83:474–478.
7. Kurtzman SH, Russo A, Mitchell JB, et al. $^{212}$Bi linked to an antipancreatic carcinoma antibody: model for alpha-particle-emitter radioimmunotherapy. *J Natl Cancer Inst.* 1988;80:449–452.
8. Macklis RM, Kinsey BM, Kassis AI, et al. Radioimmunotherapy with alpha-particle-emitting immunoconjugates. *Science.* 1988;240:1024–1026.
9. Harrison A, Royle L. Efficacy of astatine-211-labeled monoclonal antibody in treatment of murine T-cell lymphoma. *NCI Monogr.* 1987;3:157–158.
10. Kassis AI, Harris CR, Adelstein SJ, Ruth TJ, Lambrecht R, Wolf AP. The in vitro radiobiology of astatine-211 decay. *Radiat Res.* 1986;105:27–36.
11. Zalutsky MR, Garg PK, Friedman HS, Bigner DD. Labeling monoclonal antibodies and F(ab')2 fragments with the alpha-particle-emitting nuclide astatine-211: preservation of immunoreactivity and in vivo localizing capacity. *Proc Natl Acad Sci USA.* 1989;86:7149–7153.
12. Zalutsky MR, McLendon RE, Garg PK, Archer GE, Schuster JM, Bigner DD. Radioimmunotherapy of neoplastic meningitis in rats using an alpha-particle-emitting immunoconjugate. *Cancer Res.* 1994;54:4719–4725.
13. Geerlings MW. Radionuclides for radioimmunotherapy: criteria for selection. *Int J Biol Markers.* 1993;8:180–186.
14. Kaspersen FM, Bos E, Doornmalen AV, Geerlings MW, Apostolidis C, Molinet R. Cytotoxicity of $^{213}$Bi- and $^{225}$Ac-immunoconjugates. *Nucl Med Commun.* 1995;16: 468–476.
15. McDevitt MR, Sgouros G, Finn RD, et al. Radioimmunotherapy with alpha-emitting nuclides. *Eur J Nucl Med.* 1998;25:1341–1351.
16. McDevitt MR, Finn RD, Sgouros G, Ma D, Scheinberg DA. An $^{225}$Ac/$^{213}$Bi generator system for therapeutic clinical applications: construction and operation. *Appl Radiat Isotopes.* 1999;50:895–904.
17. Nikula TK, McDevitt MR, Finn RD, et al. Alpha-emitting bismuth cyclohexylbenzyl DTPA constructs of recombinant humanized anti-CD33 antibodies: pharmacokinetics, bioactivity, toxicity and chemistry. *J Nucl Med.* 1999;40:166–176.
18. Jurcic JG, McDevitt MR, Sgouros G, et al. Targeted alpha-particle therapy for myeloid leukemias: a phase I trial of bismuth-213-HuM195 (anti-CD33) [abstract]. *Blood.* 1997; 90(suppl):504a.
19. Scheinberg DA, Tanimoto M, McKenzie S, Strife A, Old LJ, Clarkson BD. Monoclonal antibody M195: a diagnostic marker for acute myelogenous leukemia. *Leukemia.* 1989;3:440–445.
20. Tanimoto M, Scheinberg DA, Cordon-Cardo C, Huie D, Clarkson BD, Old LJ. Restricted expression of an early myeloid and monocytic cell surface antigen defined by monoclonal antibody M195. *Leukemia.* 1989;3:339–348.
21. Caron PC, Jurcic JG, Scott AM, et al. A phase 1B trial of humanized monoclonal antibody M195 (anti-CD33) in myeloid leukemia: specific targeting without immunogenicity. *Blood.* 1994;83:1760–1768.
22. Scheinberg DA, Lovett D, Divgi CR, et al. A phase I trial of monoclonal antibody M195 in acute myelogenous leukemia: specific bone marrow targeting and internalization of radionuclide. *J Clin Oncol.* 1991;9:478–490.
23. Schwartz MA, Lovett DR, Redner A, et al. Leukemia cytoreduction and marrow ablation after therapy with $^{131}$I labeled monoclonal antibody M195 for acute myelogenous leukemia (AML). *J Clin Oncol.* 1993;11:294–303.
24. Sgouros G, Graham MC, Divgi CR, Larson SM, Scheinberg DA. Modeling and dosimetry of monoclonal antibody M195 (anti-CD33) in acute myelogenous leukemia. *J Nucl Med.* 1993;34:422–430.
25. Junghans RP, Sgouros G, Scheinberg DA. Antibody-based immunotherapies for cancer. In: Chabner B, Longo DL, eds. *Cancer Chemotherapy and Biotherapy: Principles and Practice.* 2nd ed. Philadelphia, PA: Lippincott; 1996:655–689.
26. Cole A. Absorption of 20-eV to 50,000-eV electron beams in air and plastic. *Radiat Res.* 1969;38:7–33.
27. Browne E, Firestone RB, Shirley VS. *Table of Radioactive Isotopes.* New York, NY: John Wiley & Sons; 1986.
28. Sgouros G, Humm JL, McDevitt M, et al. Bisumth-213 imaging: pre-clinical characterization of an alpha-particle emitting radionuclide [abstract]. *J Nucl Med.* 1996;37:78P–79P.
29. Jaszczak RJ, Greer KL, Floyd CE Jr, Harris CC, Coleman RE. Improved SPECT quantification using compensation for scattered photons. *J Nucl Med.* 1984;25:893–900.
30. Koral KF, Wang X, Rogers WL, Clinthorne NH, Wang X. SPECT: Compton-scattering correction by analysis of energy spectra. *J Nucl Med.*1988;29:195–202.
31. Hubbell JH, Seltzer SM. Tables of x-ray mass attenuation coefficients and mass energy-absorption coefficients 1 keV to 20 MeV for elements Z = 1 to 92 and 48 additional substances of dosimetric interest. National Institute of Standards and Technology 5632, Web version 1.02, 1997. Available at: http://www.physics.nist.gov/PhysRefData/XrayMassCoef/cover.html. Accessed October 12, 1999.
32. International Commission on Radiological Protection. *Report of the Task Group on Reference Man.* ICRP publication 23. New York, NY: Pergamon Press; 1975:86–91.
33. Loevinger R, Budinger TF, Watson EE. *MIRD Primer for Absorbed Dose Calculations.* New York, NY: Society of Nuclear Medicine; 1989.
34. Snyder WS, Ford MR, Warner GG. *Estimates of Specific Absorbed Fractions for Photon Sources Uniformly Distributed in Various Organs of a Heterogeneous Phantom.* MIRD pamphlet no. 5, rev ed. New York, NY: Society of Nuclear Medicine; 1978.
35. Erdi YE, Mawlawi O, Larson SM, et al. Segmentation of lung lesion volume by adaptive positron emission tomography image thresholding. *Cancer.* 1997; 80(suppl):2505–2509.
36. Erdi YE, Wessels B, Loew M, Erdi A. Threshold estimation in single photon emission computed tomography (SPECT) and planar imaging for clinical radioimmunotherapy. *Cancer Res.* 1995;55(suppl):5823s–5826s.
37. Raju MR, Eisen Y, Carpenter S, Inkret WC. Radiobiology of alpha particles. III. Cell inactivation by alpha-particle traversals of the cell nucleus. *Radiat Res.* 1991;128:204–209.
38. Snyder W, Ford M, Warner G, Watson S. *'S' Absorbed Dose per Unit Cumulated Activity for Selected Radionuclides and Organs.* MIRD pamphlet no. 11. New York, NY: Society of Nuclear Medicine; 1975.
39. Larson SM, Nelp WB. The radiocolloid bone marrow scan in malignant disease. *J Surg Oncol.* 1971;3:685–697.
40. Simons RJB. Passive transport and binding of lead by human red blood cells. *J Physiol.* 1986;378:267–286.